Unveiling cellular communications through rapid pan-membrane-protein labeling

Hirushi Gunasekara [1], Yu-Shiuan Cheng [1], Vanessa Perez-Silos[2], Alejandro Zevallos-Morales [2], Daniel Abegg [1], Alyssa Burgess [1], Liang-Wei Gong[3], Richard D. Minshall [4,5], Alexander Adibekian [1,5,6,7], Carlos Murga-Zamalloa [2,5], Alison E. Ondrus [1,6] & Ying S. Hu [1,5,8] ✉

Dynamic protein distribution within and across the plasma membrane is pivotal in regulating cell communication. However, rapid, high-density labeling methods for multiplexed live imaging across diverse cell types remain scarce. Here, we demonstrate N-hydroxysuccinimide (NHS)-ester-based amine crosslinking of fluorescent dyes to uniformly label live mammalian cell surface proteins. Using model cell systems, we capture previously elusive membrane topology and cell-cell interactions. Live imaging shows transient membrane protein accumulation at cell-cell contacts and bidirectional migration patterns guided by membrane fibers in DC2.4 dendritic cells. Multiplexed super-resolution imaging reveals the biogenesis of membrane tunneling nanotubes that facilitate intercellular transfer in DC2.4 cells, and caveolin 1-dependent endocytosis of insulin receptors in HEK293T cells. 3D superresolution imaging reveals membrane topology remodeling in response to stimulation, generation of microvesicles, and phagocytic activities in Jurkat T cells. Furthermore, NHS-labeling remains stable in vivo, enabling visualization of intercellular transfer among splenocytes using a T cell lymphoma mouse model.

Direct visualization of complex 3D membrane topologies and dynamic membrane behaviors enhances our understanding of membrane-associated intercellular and intracellular communication. The exchange of information and materials within and between cells is facilitated by various mechanisms[1], including receptor-mediated signaling, diffusion of soluble mediators, formation of specialized membrane structures[2,3], and exchange of membrane-derived extracellular vesicles[4]. In recent years, cell-cell communication through material trafficking by specialized membrane protrusions has been increasingly recognized as a crucial process in diverse pathophysiological processes[5–7]. In this context, high-resolution fluorescence imaging

enables real-time analysis, while multiplexing accurately identifies the origins and destinations of membrane-derived entities, further enhancing the mechanistic understanding of these membrane-associated processes.

Whereas fluorescence microscopy offers high spatial and temporal resolution, membrane labeling techniques remain limited. Protein-specific labeling approaches often involve exogenous expression systems and biorthogonal chemistry to incorporate (chemically or enzymatically) reactive groups, such as genetically encoded tags[8–10]. These approaches require genetic modification, which is prone to perturb native protein homeostasis and limits applicability in specific

[1]Department of Chemistry, College of Liberal Arts and Sciences, University of Illinois Chicago, Chicago, IL 60607, USA. [2]Department of Pathology, College of Medicine, University of Illinois Chicago, Chicago, IL 60612, USA. [3]Department of Biological Sciences, College of Liberal Arts and Sciences, University of Illinois Chicago, Chicago, IL 60607, USA. [4]Departments of Anesthesiology & Pharmacology and Regenerative Medicine, College of Medicine, University of Illinois Chicago, Chicago, IL 60612, USA. [5]University of Illinois Cancer Center, Chicago, IL 60612, USA. [6]Department of Pharmaceutical Sciences, College of Pharmacy, University of Illinois Chicago, Chicago, IL 60612, USA. [7]Department of Biochemistry and Molecular Genetics, College of Medicine, University of Illinois Chicago, Chicago, IL 60607, USA. [8]Department of Biomedical Engineering, Colleges of Engineering and Medicine, University of Illinois Chicago, Chicago, IL 60607, USA. ✉e-mail: yshu@uic.edu

cell types. Direct biorthogonal labeling procedures combined with metabolic labeling are time-consuming[11,12] and may not be easily adaptable to primary cells. In contrast, unbiased chemical labeling of all membrane proteins (pan-membrane-protein labeling) enables rapid and straightforward labeling for live-cell imaging. Currently, Mem-Brite™ Fix stains (Biotium) represent a commercial option for labeling membrane proteins[13]. However, the labeling mechanism is proprietary, and the selection of dyes is limited.

In this work, we identify a rapid labeling strategy amenable to live-cell imaging with well-defined chemistry for superresolution and multiplexed imaging. In this regard, we use N-hydroxysuccinimide (NHS)-ester-activated small molecule organic dyes to label membrane proteins through primary amines (R-NH$_2$)[14-17] in mammalian cells. While the technique has been successfully demonstrated for labeling live bacterial cell outer membranes[17], total protein labeling of fixed cells for expansion microscopy applications (pan-ExM)[15], tissue labeling of extracellular matrix proteins[18,19], and dye internalization-based subcellular organelle labeling[16], applications for live mammalian cell membranes have not been described.

Here, we demonstrate NHS-ester-based membrane protein labeling of live mammalian cells. We employ standard total-internal-reflection fluorescence (TIRF) microscopy as well as advanced multi-spot 3D structured illumination microscopy (SIM) to demonstrate the versatility of the labeling technique. We resolve the fine structures of the plasma membrane and membrane-derived structures in various live-cell, multiplexed, volumetric, and in vivo settings, highlighting the versatility and efficacy of this labeling strategy as a valuable tool to elucidate cell membrane and membrane-associated intercellular and intracellular communications.

Results

NHS-ester-based membrane-protein labeling achieves rapid, high-density labeling and enables visualization of dynamic cell shapes and membrane proteins

NHS-ester-activated labeling compounds react readily with cell surface proteins containing exposed amine groups, forming a chemically stable amide bond, which covalently couples the labeling molecule to the protein (Fig. 1a). The rapid reactivity of NHS-esters allows for quick labeling of cell surface proteins, typically within 5 min, facilitating efficient live cell labeling while minimizing passive dye internalization (Fig. 1b). In a proof-of-concept experiment, we demonstrated the compatibility of NHS-ester chemistry with pan-membrane-protein labeling for live cell imaging by labeling mouse dendritic cells (DC2.4) in suspension with Alexa Fluor 647 NHS-ester (AF647-DC2.4) and imaging the labeled cells landed on 8-well chambered cover glass using TIRF microscopy. Figure 1c shows the overall live cell shape defined by the membrane labeling. Next, we compared the degree of cell surface labeling of AF647-DC2.4 to a standard lipophilic dye, DiO. In our hands, DiO labeling exhibited heterogeneous membrane staining, where only a fraction of the labeled cells was visible under TIRF illumination (Fig. 1d)[13,20]. In contrast, the NHS-ester-based labeling was evident in all cells, likely due to covalent and unbiased primary amine conjugation to the cell surface (Fig. 1d and Supplementary Fig. 1).

To assess extracellular membrane labeling, we employed trypan blue, a reagent previously demonstrated to quench extracellular fluorescence[16,21]. Figure 1e, f show the fluorescent images of the labeled cells before and after the trypan blue treatment. The 50–80% reduction in fluorescence intensity (Fig. 1g) supports the notion that labeled proteins are primarily localized on the extracellular side of the cell membrane. Moreover, while membrane proteins are the predominant source of free amines, membrane phospholipids such as phosphatidylethanolamine (PE) may also contribute to free primary amine labeling. To evaluate the specificity of NHS-ester labeling to proteins, fixed and labeled DC2.4 were treated with a chloroform, methanol and acetic acid solution (CHCl$_3$/MeOH/AcOH 10:55:0.75) for lipid

extraction and washing[22,23]. Membrane labeling remained largely intact following the organic solvent washing step, indicating that the observed NHS-ester labeling is primarily contributed by proteins (Supplementary Fig. 2). Importantly, the NHS-ester-based labeling achieves efficient labeling across diverse membrane proteins, thereby enabling uniform pan-membrane-protein labeling. To confirm the labeling efficiency, we performed a comparison between the plasma membrane protein fraction and the NHS-biotin-labeled fraction using DC2.4 cells as a model system analyzed by liquid chromatography-mass spectrometry. The proteomic analysis identified 585 plasma membrane proteins (Supplementary Table 1), where the NHS-biotin-labeled proteins exhibited a 91.3% overlap with the plasma membrane proteome (Fig. 1h). This proteomics analysis suggests that rapid NHS-ester labeling captures the majority of plasma membrane proteins.

High-density membrane protein labeling enables extended live-cell imaging, revealing detailed cell shape and migration dynamics. Using DC2.4 cells imaged through TIRF microscopy, we observed that cells reversed their migratory direction within ~1.5 h, guided by their membrane fibers (Fig. 1i, orange dashed-line arrow, and Supplementary Movie 1). Figure 1j and Supplementary Movie 2–3 show a representative event where a DC2.4 cell (marked cell 1) establishes transient contact with another DC2.4 cell (marked cell 2) via its membrane fibers. Following this interaction, cell 1 reverses its direction of migration. Furthermore, pan-membrane-protein labeling enables visualization of dynamic proteome redistribution within the plasma membrane, i.e., during membrane contact in cell-cell communication. Notably, as cell 1 approached cell 2, its basal membrane protein density increased (Fig. 1j, 00:54:20), and then declined as cell 1 moved away (Fig. 1j, 01:46:10). Similar basal membrane protein redistribution dynamics were observed when cell-cell contact was initiated at the cell body and returned to its original path (Supplementary Fig. 3 and Supplementary Movie 4). Given that the pan-membrane-protein labeling was performed prior to the cell landing on glass, the enrichment of membrane proteins at cell-cell contact sites is unlikely due to the preferential labeling of proteins. The ability to stably resolve membrane fibers and the protein dynamics within these structures is likely attributed to the high-density labeling of the membrane proteins.

Multiplexed pan-membrane-protein labeling reveals material transfer between DC2.4 via membrane nanotubes

A key advantage of pan-membrane-protein labeling is its ease of multiplexing. This approach enables color-coded membrane structures to differentiate donor and recipient cells, particularly in fine membrane connections between cells. To demonstrate this capability, we labeled two separate DC2.4 populations with NHS-AF647 and Alexa Fluor 488 NHS-ester (NHS-AF488) and imaged them after a 2 h co-culture at a 1:1 ratio (Fig. 2a). We observed directional protein trafficking along membrane fibers that resemble tunneling nanotubes (TNTs), reported previously[2,5,24,25]. We monitored the transfer of a membrane-derived particle from the green cell (AF647-DC2.4) to the magenta cell (AF488-DC2.4) over the course of 1 h (Supplementary Movie 5). Figure 2b, c show representative time points from this process, illustrating the movement of the AF647-DC2.4 membrane-derived particle (white arrowhead) toward the magenta cell with the direction of transfer indicated by the arrow. Zoomed-in views in Fig. 2c highlight the specific time points of the transfer process, spanning ~10 min.

The trafficked particle demonstrates a phase of intermittent bidirectional movement, followed by a transition to steady, unidirectional motion toward the AF488-labeled DC2.4 cell, where it is ultimately internalized. The bidirectional motion characteristic resembles cargoes transported by microtubule-associated proteins through thick TNTs (diameter >0.7 μm)[3,25]. In addition, similar dynamic behavior has been described for bacterial pathogens and surface-bound nanobeads transported along thin TNTs (diameter <0.7 μm) in macrophages
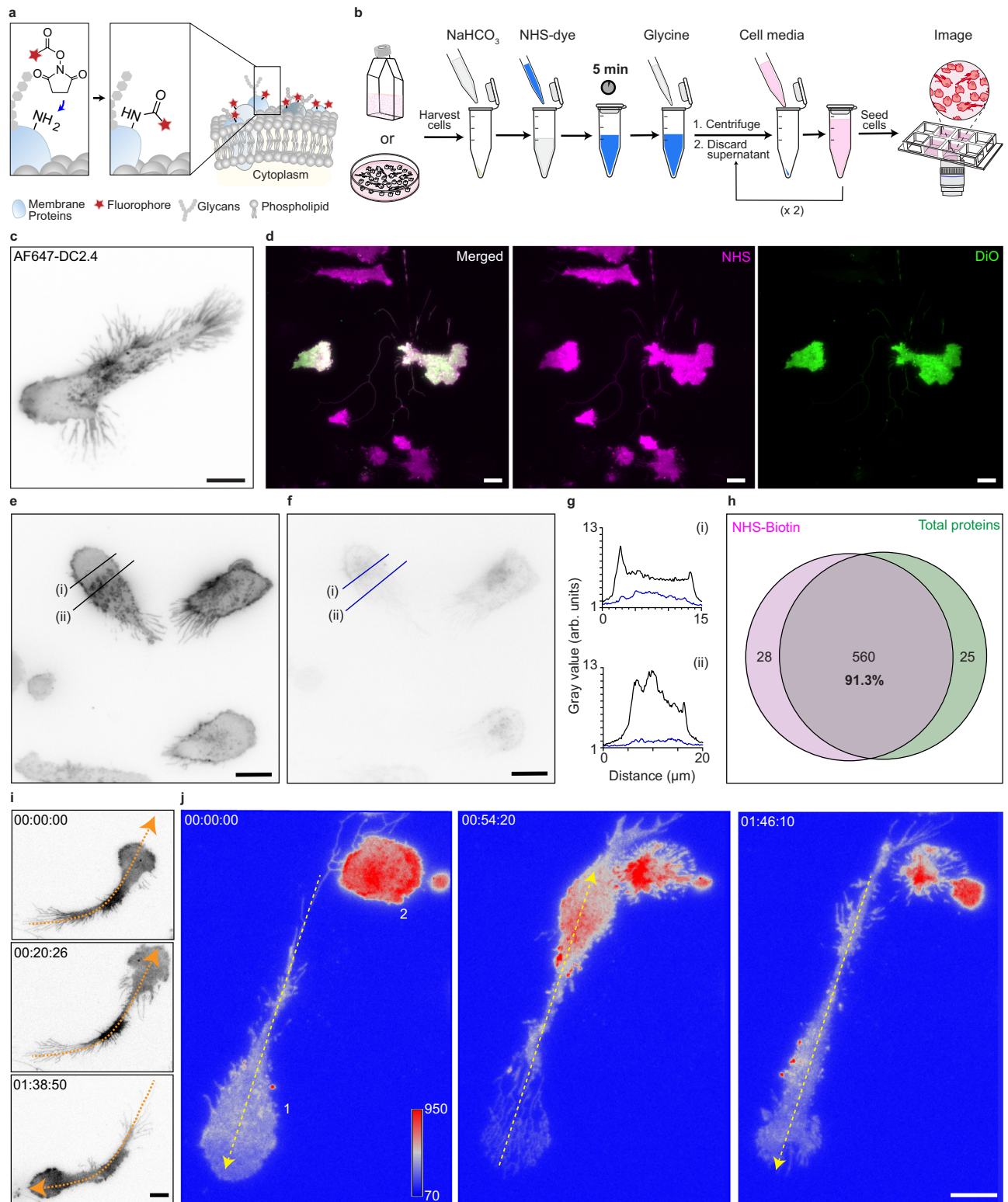
through membrane surfing[26], a mechanism where the constitutive flow of membrane components along the nanotube surface causes transient bidirectional movement but ultimately resolves into unidirectional trafficking toward one of the connected cells. Our observations align with previous reports of material exchange dynamics via TNTs[3,5,26] and suggest that DC2.4 utilizes similar mechanisms. Interestingly, membrane-derived particle trafficking was detected along branched membrane fibers that were not engaged in directly connecting adjacent cells (Supplementary Fig. 4a–d) with diverse kinetics

(Supplementary Movies 6–9). Similar patterns of material trafficking in DC2.4 branched membrane protrusions have been shown using polyacrylic acid-coated quantum dots[27], suggesting DC2.4 cells employ specialized membrane fibers for material uptake and trafficking. Moreover, NHS-ester labeled membrane proteins were detected within the cytoplasm of cells labeled with a different color, demonstrating the prevalence of material exchange between the two cell populations (Fig. 2d). Because the amide bond formed during NHS-ester cross-linking is highly stable and irreversible under physiological

Fig. 1 | NHS-ester-based amine-reactive chemistry enables rapid, uniform, and high-density protein labeling for prolonged live imaging of the cell membrane. **a** The general principle of membrane protein labeling via *N*-hydroxysuccinimide (NHS) ester chemistry. The NHS-dye ester is covalently coupled to the exposed amine groups of proteins on the outer surface of cells. **b** The schematic illustration of the procedural steps for NHS-ester-dye labeling of live cells in suspension within 5 min. **c** The total-internal-reflection fluorescence (TIRF) image of a DC2.4 cell labeled with AF647 NHS-ester. **d** DiO labeling results in heterogeneous membrane staining. The merged TIRF images of the DC2.4 cells co-labeled with DiO and NHS-AF647 (left) and the single color TIRF images (right). The NHS-ester labeling is shown in magenta, DiO labeling is shown in green and colocalized cells appear in white. **e** A representative TIRF image of dendritic cells labeled for proteins with NHS-AF647. **f** TIRF images of the same region in (**e**) in the presence of trypan blue. **g** Intensity line profiles across lines before (black solid line) and after exposure

(blue solid line) to trypan blue marked as i-ii in (**e**, **f**). arb. units refer to arbitrary units. **h** Venn diagram showing the overlap between plasma membrane proteins enriched with NHS-ester-biotin vs. total plasma membrane proteins, indicating that 91.3% of the membrane proteins are labeled by NHS-ester conjugation (*n* = 3 technical replicates). **i** Representative images from a time-lapse video showing DC2.4 cells reversing the direction of migration by expanding their retraction fibers. Time points are presented in the format hh:mm:ss. The orange dashed line indicates the direction of their migration. The complete image sequences are shown in Supplementary Movie 1. **j** Representative images from a time-lapse video captured a DC2.4 cell (marked cell 1) contacting another DC2.4 cell (marked cell 2). The yellow dashed line indicates the direction of migration. The color bar represents image intensity (arbitary units). The complete image sequences are shown in Supplementary Movie 2-3. Scale bars: 10 μm.
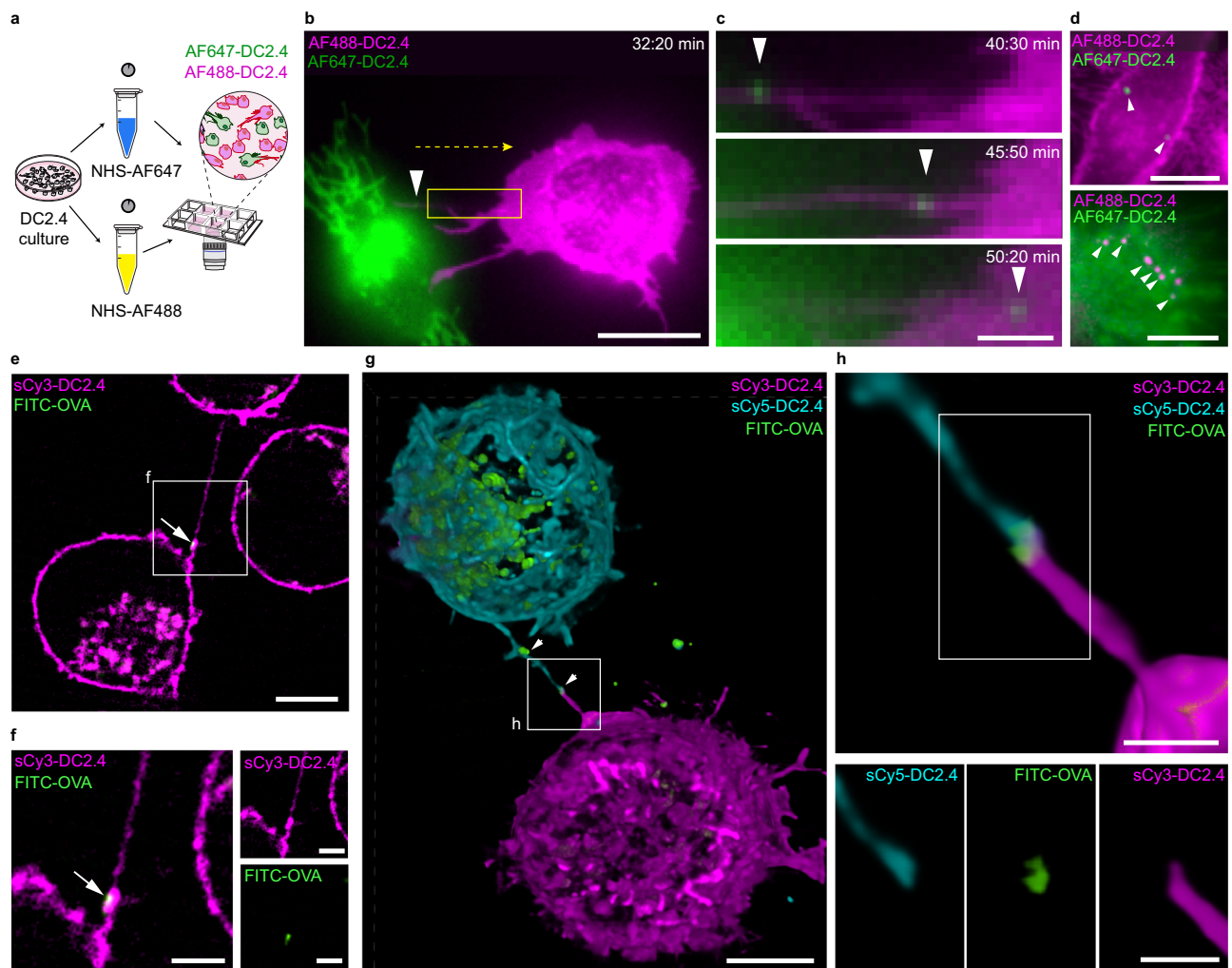
Fig. 2 | Multiplex pan-membrane-protein labeling enables visualization of intercellular DC2.4 communication through membrane tunneling nanotubes. **a** Schematic illustration of the dual-color labeling experiment with AF647 (green) and AF488 (magenta). **b** Dual-color pan-membrane-protein labeling enables the visualization of material transfer between DC2.4. The white arrowhead points to an AF647-DC2.4 membrane-derived particle. The yellow dashed arrow indicates the direction of transport. Time points are presented in the format mm:ss. **c** Zoomed-in images from the boxed region in (**b**) showing the time-lapse sequence of the transfer. The white arrowhead follows the transported particle. Image contrast is adjusted in each subpanel to highlight the transfer process. The full image sequence is available in Supplementary Movie 5. **d** The material exchange between AF488-DC2.4 (magenta) and AF647-DC2.4 (green) is observed

after a 2 h co-culture. White arrowheads point to the non-self-colored membrane-derived particles detected within the cells. **e** 2D SIM image of FITC-OVA (green) along a TNT (white arrow) connecting two DC2.4 cells (magenta). **f** Zoomed-in views of the boxed region indicated on (**e**) (left) and the individual channels (right). **g** A multiplexed volumetric SIM image shows the biogenesis of TNTs in the presence of FITC-OVA. Volumetric DeepSIM image of a FITC-OVA (green) laden sCy5-DC2.4 cell (cyan) interacting with a sCy3-DC2.4 (magenta) via a TNT. White arrowheads point to the FITC-OVA observed along the TNT. **h** Zoomed-in image of the boxed region indicated in (**g**) (top) and the single-color images of sCy5-DC2.4, FITC-OVA, and sCy3-DC2.4 (bottom). Representative images from two independent experiments (**e**–**h**) are shown. Scale bars: 10 μm (**b**, **d**), 2 μm (**c**, **f**), 5 μm (**e**, **g**) and 1 μm (**h**).

conditions[28], the observed transferred materials are likely membrane-derived particles carrying NHS-ester labeled proteins.

In addition, pan-membrane-protein labeling is compatible with fluorescently labeled ligands, enabling the study of their interactions with target cells. To this end, we co-cultured DC2.4 cells labeled separately with sulfo-Cyanine3 (sCy3) and sulfo-Cyanine5 (sCy5) NHS-esters in the presence of FITC-labeled ovalbumin (FITC-OVA), a common protein used as a soluble antigen to study antigen presentation[29,30]. We employed a multi-spot structured illumination microscope (DeepSIM, CrestOptics) to resolve the spatial relationship between FITC-OVA and the DC2.4 membrane. Within 3 h of co-culture, we observed the presence of FITC-OVA on TNTs and branched membrane fibers (Fig. 2e, f and Supplementary Fig. 4e, f). In addition, volumetric imaging revealed the intracellular distribution of FITC-OVA (Fig. 2g). The sCy5-DC2.4 cell shows a greater degree of intracellular FITC-OVA than the sCy3-DC2.4 cell, suggesting intra-population heterogeneity in FITC-OVA uptake by DC2.4. Interestingly, we observed the formation of a dual-colored TNT between two interacting DC2.4 cells, with one cell labeled with sCy3 and the other labeled with sCy5. Each cell contributed a portion to the structure of the TNT (Fig. 2g). Moreover, FITC-OVA was identified at the junction between two connecting ends of the TNT (Fig. 2h). These imaging results demonstrate the capability of our membrane labeling strategy to reveal the biogenesis of TNT and its involvement in intercellular communication. The understanding of the biogenesis of TNTs is limited as these structures are highly dynamic and fragile, with limited options to label them for live-cell characterizations[31,32]. Our NHS-ester based pan-membrane-protein labeling technique thus provides a versatile tool to study their dynamics in live cells under pathophysiological conditions.

Pan-membrane-protein labeling combined with fluorescent fusion proteins enables the monitoring of endocytic pathways

In addition to fluorescently tagged protein ligands, the NHS-ester-based pan-membrane-protein labeling strategy can be integrated with fluorescent fusion proteins to monitor endocytic activities at the plasma membrane. We demonstrate this capability through the endogenous endocytic activity of DC2.4 cells and insulin receptor endocytosis triggered by insulin binding in HEK293T cells.

Caveolae represent vesicular structures internalized from the cell membrane involved in membrane internalization and recycling[33,34] and antigen uptake in dendritic cells[34–36]. Based on this, we reasoned that the endocytosed labeled membrane would be transported through the endosomal network to late endosomes and lysosomes overtime via the caveolin-dependent pathway. To test this possibility, we performed pan-membrane-protein labeling in separate DC2.4 cultures expressing either caveolin 1 (Cav1, caveolin-dependent endocytosis marker) fused to mCherry, Rab7 (late endosome marker) fused to mScarlet, and lysosomal-associated membrane protein 1 (LAMP1, lysosome marker) fused to mCherry in. We also transfected a DC2.4 culture with mitoDsRed2 (mitochondria marker) as a negative control to evaluate the potential labeling of subcellular organelles during NHS-ester labeling. Figure 3a shows the dual-color images of the pan-membrane-protein labeled DC2.4 cells expressing fluorescently fused Cav1, Rab7, LAMP1, or mitoDsRed2 4 h after pan-membrane-protein labeling. Figure 3b shows the magnified view as well as separate color channels. NHS labeling overlaps between the internalized membrane label (green) and Cav1 (magenta) with a Pearson correlation coefficient of 0.39 ± 0.047 (mean $\pm$ SEM, $n = 12$ cells, one ROI per cell) (Fig. 3c and Supplementary Fig. 5). The observation supports the notion that caveolin-dependent endocytosis is involved in the internalization of the membrane label in DC2.4 cells. Furthermore, a sub-population of Rab7 (magenta) and LAMP1 (magenta) colocalize with the membrane label (green) with Pearson correlation coefficients of 0.54 ± 0.016 (mean $\pm$ SEM, $n = 18$ cells, one ROI per cell) and 0.50 ± 0.028 (mean $\pm$ SEM, $n = 11$ cells, one ROI per cell), respectively (Fig. 3c and

Supplementary Figs. 6–7). In contrast, NHS-ester labeling showed anti-correlation with mitoDsRed2 (-0.16 ± 0.019, $n = 12$ cells, one ROI per cell) (Fig. 3c and Supplementary Fig. 8), suggesting that the NHS-ester did not label or accumulate in mitochondria. The colocalization data further demonstrate that at 4 h post membrane labeling, some original labeled membrane proteins have left the membrane through endocytic recycling pathways in DC2.4 cells.

Next, we investigated Cav1-mediated insulin receptor (InsR) endocytosis in HEK293T cells. Insulin has been shown to dose-dependently trigger caveolin-dependent endocytosis of InsR in vitro[37,38]. Cav1 phosphorylation modulates InsR internalization, with phosphorylation promoting InsR endocytosis. To monitor Cav1-dependent InsR internalization, we employed NHS pan-membrane-protein labeling of HEK293T cells stimulated with insulin. We co-expressed mCherry-fused Cav1 wildtype or a dominant-negative non-phosphorylatable mutant at tyrosine 14 (Y14F)[39,40] along with EGFP-fused InsR. We performed sCy5-NHS-ester pan-membrane-protein labeling immediately prior to insulin treatment so that internalization of membrane label and subsequent intracellular colocalization with InsR and Cav1 could serve as a readout for insulin-stimulated InsR endocytosis. 2D SIM microscopy reveals a minimal level of basal InsR endocytosis in the absence of insulin treatment (Fig. 3d and f). Upon stimulation with insulin, cells expressing Cav1-WT exhibited InsR endocytosis marked by the internalized NHS label (Fig. 3e and g). NHS labeling colocalizes with InsR-GFP and Cav1, further highlighting Cav1-dependent InsR endocytosis (Fig. 3h). In contrast, cells expressing the dominant-negative Cav1-Y14F mutant showed little responsiveness to insulin treatment (Fig. 3e, g, and i). These findings align with previous studies indicating that Cav1 phosphorylation is required for InsR internalization. Owing to the stable and uniform labeling of the cell membrane, these results demonstrate the utility of pan-membrane-protein labeling for visualizing endocytic activities and subsequent vesicular trafficking within cells.

3D SIM reveals membrane dynamics and materials transfer across the plasma membrane of T cells

The high membrane labeling density further enables volumetric superresolution imaging of the 3D membrane topology and dynamics of fine membrane structures. To establish this capability, we used Jurkat T cells (clone E6.1), which feature a large nucleus and significant height compared to DC2.4 and HEK293T cells. First, we demonstrated that Jurkat T cells exhibit distinct 3D membrane topologies when they come into contact with different ligand-coated glass surfaces. Figure 4a shows Jurkat membranes on a non-activating surface coated with poly-L-lysine (PLL) from bottom-up and top-down perspectives. The 3D SIM images capture membrane microvilli[41] (Fig. 4b (i) Supplementary Movie 10) and segregated membrane protein distributions on the top of the cell (Fig. 4b (ii) and Supplementary Movie 10). Figure 4c and Supplementary Movie 11 show a distinct T cell membrane on a stimulating surface coated with anti-CD3 (OKT-3) antibodies, featuring membrane ruffles (Fig. 4d (i))[41]. In addition, the apical membrane protein topology is distinct compared to the part of the T cell resting on the non-activating surface (Fig. 4d (ii) vs. Fig. 4b (ii)). Live-cell volumetric superresolution imaging of Jurkat T cells shows dynamic probing of the PLL glass surface without entirely flattening the cell membrane (Supplementary Fig. 9a and Supplementary Movie 12). In contrast, the Jurkat T cell is fully attached to the OKT-3 surface, as evidenced by the settling of membrane ruffles at the cell periphery (Supplementary Fig. 9b and Supplementary Movie 13). Membrane protein clusters near the initial contact site diminish over time, while their accumulation increases at the membrane ruffles (Supplementary Movies 13). In addition, upon prolonged activation (>1 h) on the OKT-3 surface, we observe the presence of membrane-derived extracellular vesicles (EVs) on the glass surface (Fig. 4e). This observation is consistent with previous reports on microvesicle release from T cells[6,41,42].
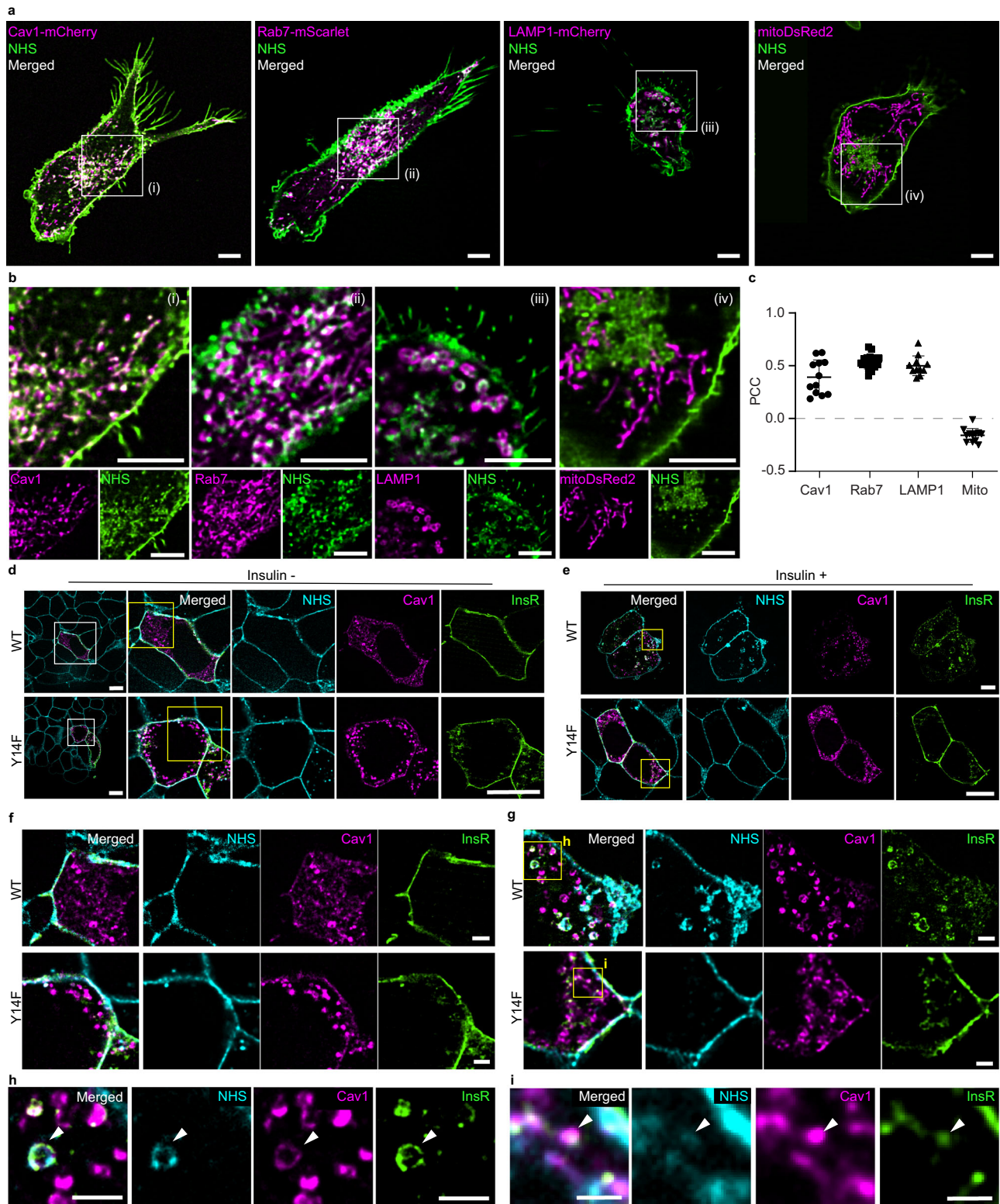
Interestingly, the protein distribution around the EVs displays uneven patterns (Fig. 4f), with EVs ranging from ~0.2 to 1.6 µm at their widest point (Fig. 4g, h).

In addition, Jurkat T cells exhibited phagocytic activities toward Dynabeads (4.5 µm, CD3/CD28 coated) when immobilized on a PLL surface. Supplementary Fig. 9c and Supplementary Movie 14 show the brightfield and fluorescent images and videos of a representative event. Supplementary Movie 15 shows the representative volumetric superresolution video. As shown in zoomed-in views in Fig. 4i,

membrane ruffles start forming a phagocytic cup around one of the two Dynabeads at 0 min. By 2 min, a phagocytic cup is distinctly visible around the bead (Fig. 4i). The membrane completely encloses the Dynabead by 4 min, and the internalization of the bead is marked by a transfer of the pan-membrane-protein labeled cell membrane onto the bead (Fig. 4i, indicated by the white arrowhead). The Jurkat T cell internalizes the bead closer to the cell (marked by the white arrowhead in Fig. 4i) while leaving the other outside (indicated by the yellow arrowhead in Fig. 4i). While immobilizing cells and Dynabeads on a 2D

Fig. 3 | Pan-membrane-protein labeling combined with fluorescent fusion proteins enables the visualization of endocytic proteins involved in intracellular membrane transport. a Representative DeepSIM images of pan-membrane-protein labeled (NHS, green) DC2.4 cells with respective transfected organelle markers, Cav1, Rab7, LAMP1 and mitoDsRed2 (magenta). Colocalizations appear in white. Images were taken 4 h after pan-membrane-protein labeling. **b** Zoomed-in views of the indicated regions (i-iv) indicated in **a** (top) and the single-color images of corresponding transfected organelle marker and NHS pan-membrane-protein labeling (bottom). **c** Pearson correlation coefficient (PCC) showing the degree of colocalization of the organelle markers and the internalized NHS-ester label. Error bars represent mean and SEM. *n* = *12, 18, 11,* and *12* cells across two independent experiments for Cav1, Rab7, LAMP1, and MitoDsRed2, respectively. **d** DeepSIM microscopy images of NHS pan-membrane-protein labeled HEK293T cells (cyan) co-expressing EGFP fused InsR (green) and mCherry fused WT Cav1 or Y14F mutant Cav1 (magenta). The entire image field (left), zoomed-in merge view, and individual channels of the boxed region indicated in white (right). **e** DeepSIM microscopy images of NHS pan-membrane-protein labeled HEK293T cells (cyan) expressing EGFP fused InsR (green) and mCherry fused Cav1-WT and Cav1-Y14F (magenta) treated with 200 nM insulin for 1 h. The merged view (left) and individual channels of the boxed region indicated in white (right). **f** Zoomed-in views of the yellow-boxed regions indicated in (**d**). Merged view (left) and individual channels (right). **g** Zoomed-in views of the yellow-boxed regions indicated in (**e**). Merged view (left) and individual channels (right). **h** Colocalization of pan-membrane-protein labeling (cyan) with InsR (green) and Cav1 WT (magenta). Zoomed-in view of the yellow-boxed regions indicated in (**g**). Merged view (left) and individual channels (right). Colocalizations appear in white. **i** Colocalization of pan-membrane-protein labeling (cyan) with InsR (green) and Cav1-Y14F (magenta). Zoomed-in view of the yellow-boxed regions indicated in (**g**). Merged view (left) and individual channels (right). Colocalizations appear in white. Representative images from two independent experiments (**d**–**i**) are shown. Scale bars: 5 μm (**a**, **b**), 10 μm (**d**, **e**), 2 μm (**f**–**h**), 1 μm (**i**).

glass surface likely facilitated the phagocytic activity of the T cell, our observations demonstrate the versatility of our pan-membrane-protein labeling approach in visualizing intricate membrane dynamics. The ability to image fine membrane structures without significant photobleaching is likely attributed to homogenous and high-density labeling.

Membrane protein transfer from primary T cell lymphoma splenocytes to healthy splenocytes is evident following lymphoma cell transfer in vivo

Our data presented so far strongly suggests that our NHS-ester pan-membrane-protein labeling technique may serve as a powerful tool to study cellular communication within and between cells in culture. Next, we explored the compatibility of pan-membrane-protein labeling with primary cells and in vivo environments. To this end, we investigated the extent to which murine-derived lymphoma T cells can transfer membrane materials to the splenocytes of recipient healthy mice. We labeled bulk spleen single-cell suspensions derived from donor mice upon the spontaneous development of T cell lymphomas[43] (*SNF5*^fl/fl, CD4-Cre^{+/-} mouse on a C57/BL6 background) with sCy3 and sCy5. Subsequently, we injected the labeled cells into healthy mice (wild type C57/BL6) (Fig. 5a). Labeling two distinct cell populations minimizes false-positive readouts. Consistent with previous studies, neoplastic T cell lymphocytes will traffic and engraft in recipient spleens[44]. Therefore, we anticipated the presence of membrane-labeled lymphoma cells in the spleens of recipient mice and hypothesized the transfer of material to recipient splenocytes.

To test this hypothesis, we harvested spleens from recipient mice 24 and 48 h after injecting membrane-labeled donor cells. Recipient splenocytes were isolated from the harvested spleens and plated onto 8-well chambered cover glasses for imaging (Fig. 5a). Figure 5b shows the presence of donor cells labeled with sCy3 or sCy5 among recipient splenocytes 24 h after cell transfer. Similarly, the presence of membrane-labeled lymphoma cells can be observed 48 h after cell transfer (Fig. 5c). Intriguingly, both sCy3 and sCy5 puncta were detected from single cells lacking membrane labeling, suggesting material transfer from injected splenocytes to healthy recipient splenocytes (Fig. 5d). Furthermore, membrane markers of recipient cells can be immunostained. As *SNF5* deletion in peripheral T cells drives CD8^{+} T cell lymphoma development in the donor mouse and only neoplastic cells (CD8^{+}) are expected to engraft in recipient mice, we performed immunostaining of CD8α on recipient splenocytes as a proof-of-concept. Figure 5e shows a representative splenocyte containing both sCy3 and sCy5 puncta, but lacking pan-membrane-protein labeling and membrane CD8α staining, 48 h post-injection, further supporting the notion of material transfer to a CD8^{-} splenocyte. We also observed CD8^{+} splenocytes containing both sCy3 and sCy5 puncta without pan-membrane-protein labeling (Supplementary Fig. 10). Collectively, these results demonstrate that our NHS-ester labeling

technique enables studying intercellular communications in the in vivo environment. While further studies are needed to identify the specific nature and mechanism of NHS-tagged protein transfer in vivo, our multiplexed pan-membrane-protein labeling enables the precise identification of the source cells that generate these membrane-derived entities for further investigations.

Interestingly, the ability to rapidly label the membrane of primary cells enabled us to visualize DC2.4 cells communicating with primary CD4^{+} and CD8^{+} lymphoma T cells via TNTs in a three-color co-culture experiment (Supplementary Fig. 11 and Supplementary Movie 16). Live-cell 2D SIM imaging showed that DC2.4 cells can simultaneously maintain multiple TNTs with different cell types, and a single TNT can be accessed by multiple cell types. These findings highlight the complexity of intercellular connections mediated by specialized membrane conduits[45].

Discussion

In this study, we present an efficient membrane protein labeling strategy that utilizes NHS-ester amine-reactive chemistry. This rapid labeling approach offers a versatile, long-lasting, and high-density labeling solution for live-cell microscopy, adaptable across various cell types and applications. One of the key advantages of pan-membrane-protein labeling is its ability to provide robust labeling of the entire membrane proteome, which is particularly beneficial for prolonged live-cell imaging. Compared to standard protein-specific labeling, such as fluorescent fusion proteins, labeling of all membrane proteins combined with the more stable photophysical properties of synthetic dyes mitigates photobleaching and enables prolonged live-cell imaging (Fig. 1, and Supplementary Movies 1–3). In addition, NHS-ester-based pan-membrane-protein labeling allows for the selection of fluorophores tailored to specific applications and microscopy techniques. This versatility extends to multiplexing capabilities that can readily expand to include newly developed small molecule dyes with improved photophysical properties for live imaging, which translates to improved spatial and temporal resolution.

The high labeling density and multiplexity of NHS-ester-based pan-membrane-protein labeling enable superresolution studies of the cell membrane to reveal potentially novel modes of intercellular communication. Fine membrane structures, which are difficult to visualize due to their low labeling density and resulting low fluorescence intensity, can benefit from the enhanced sensitivity of superresolution techniques. In this work we have visualized TNTs, membrane microvilli and fibers, and membrane-derived EVs using DC2.4 (Fig. 2, Supplementary Fig. 4 and 12), Jurkat T cells (Fig. 4), and U2OS cells (Supplementary Fig. 13). While increasing evidence, including studies using electron microscopy, has revealed the physiological and pathological relevance of these membrane structures, they are challenging to capture by superresolution microscopy using
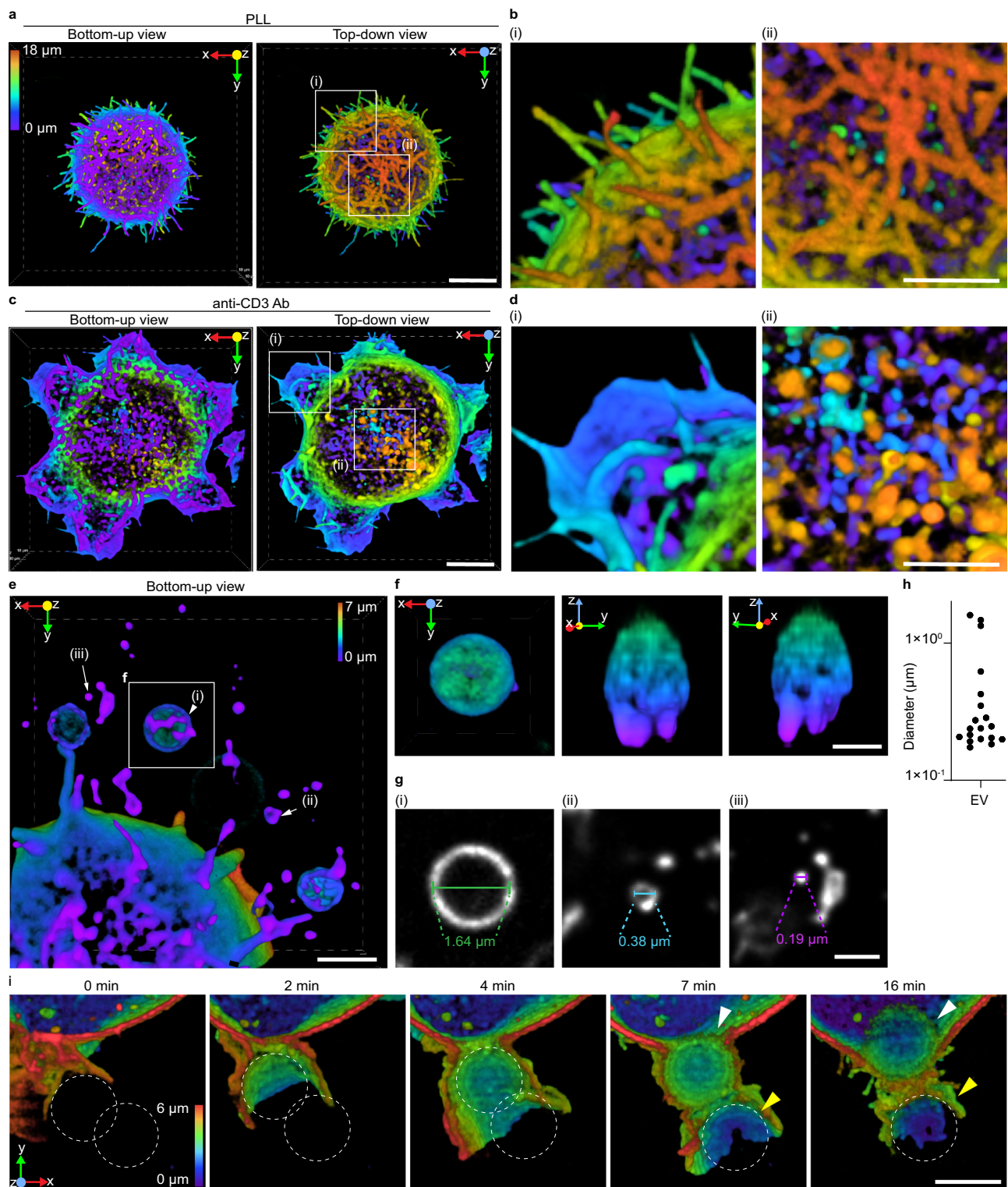
Fig. 4 | High labeling density enables the visualization of membrane protein topology of Jurkat T cells on activating glass surfaces and material transfer across the membrane through microvesicles and phagocytosis. a Representative DeepSIM volumetric superresolution image of a pan-membrane-protein labeled Jurkat T cell on a non-stimulating surface coated with poly-L-lysine (PLL). **b** Zoomed-in views of the regions indicated in (**a**) showing T cell microvilli (i) and membrane protein assemblies (ii). **c** Representative volumetric superresolution image of a pan-membrane-protein labeled Jurkat T cell on a stimulating surface coated with anti-CD3 (OKT-3) antibody. **d** Zoomed-in views of the regions indicated in (**c**) showing membrane ruffles (i) and membrane protein assemblies (ii). **e** A zoomed-in volumetric superresolution image of a pan-membrane-protein labeled

Jurkat T cell incubated for 1 h on a stimulating surface. Bottom-up view. **f** Ortho-graphic views of the indicated EV in (**e**) demonstrating volumetric membrane protein distribution. **g** The cross-sectional view of the indicated EVs in (**e**). The diameter at the widest z-position is shown on each vesicle. i: $z = 2\,\mu m$, ii: $z = 4\,\mu m$, and iii: $z = 6\,\mu m$. **h** Distribution of the extracellular vesicle (EV) diameters. $n = 19$ EVs. **i** Zoomed-in volumetric fluorescent view of the Dynabead internalization across the membrane indicated in Supplementary Fig. 9c. White arrows indicate the inter-nalized Dynabead with co-internalized membrane proteins. Yellow arrows point to a Dynabead that is not internalized. The complete image sequence is shown in Supplementary Movie 15. Scale bars: 10 μm (**a, c**), 5 μm (**b, d** and **i**), 2 μm (**e**), and 1 μm (**f, g**).
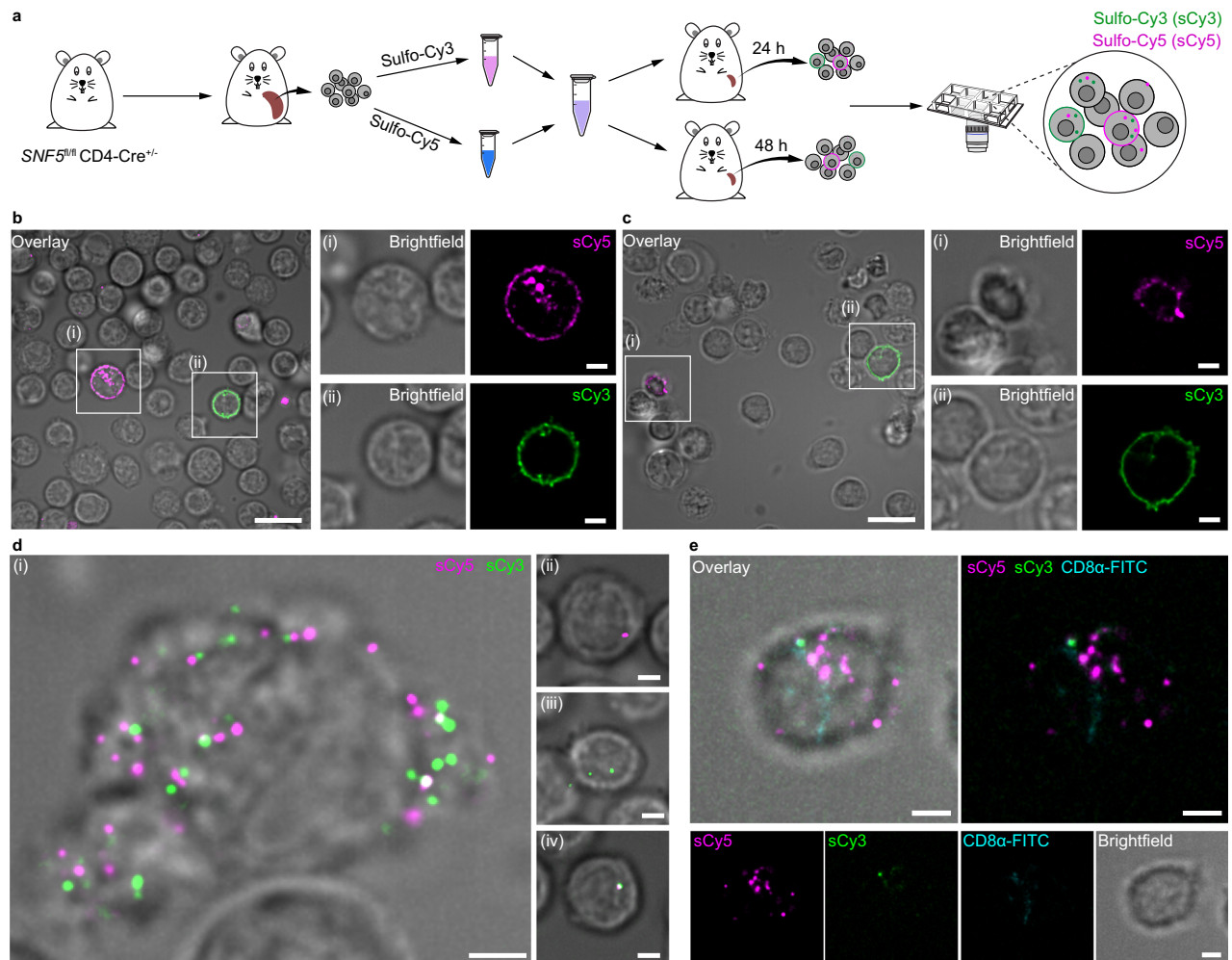
Fig. 5 | Pan-membrane-protein labeled T cell lymphoma splenocytes travel to the spleen of healthy recipient mice and exhibit material transfer with healthy splenocytes in vivo. a Schematic illustration of the in vivo material transfer experiment between spontaneously developed T cell lymphomas derived from a $SNF5^{fl/fl}$, CD4-Cre$^{+/-}$ mouse on a C57/BL6 background and bulk splenocytes from a wildtype C57/BL6 mouse. **b** Injected sulfo-Cy3 (sCy3, green) and sulfo-Cy5 (sCy3, magenta) labeled cells were detected in the recipient splenocytes 24 h post-injection. **c** Injected sulfo-Cy3 (sCy3, green) and sulfo-Cy5 (sCy5, magenta) labeled cells were also detected in the recipient splenocytes 48 h post-injection. **d** Membrane protein transfers from labeled-injected cells into recipient splenocytes. Four representative cells (i-iv) showing sulfo-Cy3 (sCy3, green) and sulfo-Cy5 (sCy5, magenta) puncta containing recipient splenocytes lacking membrane labeling. **e** Immunostaining for CD8α shows membrane transfer from the injected cells to the recipient splenocytes lacking membrane staining of CD8α-FITC. Overlay of fluorescent channels with brightfield (top left), merged fluorescent channels (top right), and individual channels (bottom). Sulfo-Cy5 (sCy5), sulfo-Cy3 (sCy3), and CD8α-FITC immunostaining is shown in magenta, green and cyan, respectively. Representative images from two technical replicates (**b**–**e**) from one independent experiment are shown. Scale bars: 10 µm (**b**, **c**, left), 2 µm (**b**, **c**: right, and **d**, **e**).

existing labeling techniques. For instance, immune cells are known to use TNTs to traffic small organelles, such as early endosomes, late endosomes, lysosomes, and multivesicular bodies within TNTs[3,25,26]. TNTs have also been shown to transfer mitochondria between various cell types, including from T cells to cancer cells to increase the metabolic activity of cancer cells while depleting the metabolic resources of immune cells[46], from bone marrow stromal cells (BMSCs) to CD8$^+$ T cells to enhance metabolic fitness and antitumor efficacy[47], and from healthy to apoptotic PC12 cells to rescue the apoptotic cells[48]. In this work, we captured a DC2.4 cell communicating with primary CD8$^+$ and CD4$^+$ lymphoma T cells using TNT-like structures (Supplementary Fig. 11 and Supplementary Movie 16). Using DiOC6(3) (3,3'-dihexyloxacarbocyanine iodide), a cell-permeant membrane potential-sensitive dye, we also observed similar intercellular mitochondria transfer between DC2.4 cells (Supplementary Fig. 14 and Supplementary Movie 17). Trafficked material may also contain small organelles where trafficking through these membrane nanotubes may be directionally controlled via

tetraspanin proteins[49], F-actin, and actin-associated motor proteins that are governed by the metabolic fitness level of the cells. Our labeling strategy enables the study of these systems in live cells using advanced fluorescence techniques. In addition, 3D superresolution imaging demands exceptionally high labeling densities. Depending on the imaging modality, including our DeepSIM system, z-sectioning inevitably results in photobleaching of the sample volume. Using Jurkat T cells as a model system for a highly structured and volumetric cell type, we demonstrate that the high labeling density of pan-membrane-protein labeling enables 3D-live cell DeepSIM imaging of cell membrane protein dynamics. This labeling strategy can be expanded to co-cultured models and thin sections of live tissue[18,19].

We show in this work that labeling of the plasma membrane proteome offers unique advantages compared to the standard lipophilic dyes in the context of in vivo studies (Fig. 1d). Standard lipophilic dyes (e.g., DiO, DiI, DiD, DiR, DiA, PKH dyes and FM dyes) integrate into the membrane through hydrophobic interactions with lipid tails. Despite

their simplicity of use, issues with staining uniformity and stability of these dyes arise due to structural differences with native lipids[13]. They are also known to undergo rapid passive diffusion, which can result in intracellular labeling and poor persistence on the cell membrane[13,20] (Fig. 1d and Supplementary Fig. 1). Indeed, the rapid internalization of these dyes is widely used to track intra- and intercellular vesicle trafficking[5,26]. Cell surface labeling can also be achieved via glycan labeling, which relies largely on lectins such as wheat germ agglutinin (WGA)[50,51] to bind specific glycans through multivalent non-covalent interactions. However, variability in glycan composition across cell types and dynamic glycan profiles in response to stimuli or cell state can complicate the application of these labels[13]. Furthermore, the non-covalent nature of the label increases the potential for dye detachment and transfer to adjacent cells, particularly for lipophilic dyes[20,52], which limits their use in multiplex imaging and in vivo investigations. In this work, we show that pan-membrane-protein labeling benefits from the covalent attachment of fluorophores to surface proteins, providing stable labeling in an in vivo environment.

While pan-membrane-protein labeling deliberately lacks specificity, we demonstrate that integrating NHS-ester-based membrane-protein labeling with fluorescent fusion proteins can enable protein-specific characterization within a global protein context (Fig. 3). Using this technique, we have visualized the requirement of caveolin 1 phosphorylation in insulin receptor internalization. The labeling strategy can be integrated with other membrane receptors and fluorescent-based assays to evaluate endocytic activities upon ligand or drug binding. Of note is that a comparison of DC2.4 cells labeled separately with NHS-ester dyes (AF488, sCy3, sCy5, and AF647) and cultured for 24 h revealed intra-population heterogeneity of endocytic activities. Among the labeled populations, some cells exhibited higher endocytic activities with significant dye accumulation in the endosomal network (Supplementary Fig. 15). These differences likely reflect the inherent heterogeneity of endocytic behavior within the cell population.

While we have demonstrated that NHS-esters enable rapid membrane labeling within minutes, it is worth noting that prolonged NHS-ester dye incubation can lead to internalization and subsequent labeling of intracellular structures, such as vesicles, mitochondria, and the endoplasmic reticulum (ER)[16]. To mitigate this, it may be possible to employ cell membrane impermeable sulfonated NHS-ester dyes[13]. However, constant membrane turnover by endocytic recycling will inevitably internalize surface labeling over time, reducing cell-surface labeling and increasing intracellular localization of the dye (Fig. 3a, b and Supplementary Fig. 15). While a trypan blue exclusion assay indicates that pan-membrane-protein labeling does not compromise cell viability (Supplementary Fig. 16), characterizations of NHS-ester-labeled live cells are best completed within 24 h post-labeling. Despite the advantages of covalent labeling, cell-to-dye ratio should be tailored and validated for specific applications to minimize functional disruptions of the cells and avoid over-labeling.

We have demonstrated the versatility of pan-membrane-protein labeling for microscopic and mass spectrometric proteomic characterizations. Our strategy could be expanded to other classical covalent chemistries, such as maleimide conjugation for thiol labeling. However, thiol labeling may interfere with disulfide bond formation and cellular responses to oxidative stress[13], requiring careful optimization for live-cell imaging. Biorthogonal chemistries, including click reactions, offer rapid and selective labeling under physiological conditions. However, these methods often require the metabolic introduction of complementary reactive groups through prolonged feeding[11,12], which may be unsuitable for primary cells. Nevertheless, careful optimization and validation of each labeling method may be applicable to live-cell imaging and functional studies.

In summary, our pan-membrane-protein labeling strategy based on NHS-ester-based covalent ligation of fluorescent dyes offers a versatile and efficient strategy for live imaging in a diverse range of cell types. The rapid labeling process, high labeling density, ease of multiplexing, and compatibility with existing fluorescent labeling approaches render this technique particularly valuable for visualizing dynamic intercellular and intracellular communication and 3D membrane dynamics at high resolution.

Methods

Ethics statement
All experimental procedures performed on mice were approved and conducted in accordance with the Animal Care Committee (ACC) at the University of Illinois Chicago (Protocol number 22-187).

Animals. *SNF5* floxed and CD4-Cre^{+/-} in C57/BL6 mice were obtained from Jackson Laboratory. Mice were backcrossed for at least five generations before starting the experiment. One 14 week-old donor mouse with spontaneous lymphoma: *SNF5*^{fl/fl}, CD4-Cre^{+/-} mouse in C57/BL6 background was used. Two 12 week-old WT C57/BL6 mice were used as recipients. All animals were housed in appropriate cages with 12 h dark and 12 h light cycles, ambient temperature, and humidity. Sex was not considered due to the proof-of-concept nature of this study.

Materials
RPMI (11875093), DMEM (11960069-500 ml, 11965118-500 ml and 11885084), penicillin-streptomycin (15140 – 122, 100 mL), DPBS (14190 – 144, 500 mL), glycine (BP381 – 500), Alexa Fluor 647 NHS ester (A37573), Alexa Fluor 488 NHS ester (A20000), Dynabead (CD3/CD28, 4.5 μm, 11161D), Vybrant™ Multicolor Cell-Labeling Kit containing DiO, DiI, DiD Solutions (V22889), DiOC6(3) (3,3'-Dihexyloxacarbocyanine Iodide, D273), Trypan Blue (15250-061), Cytiva HyClone™ HEPES Solution (SH3023701), Lipofectamine 2000 (Thermo Fisher, 11668019), Opti-MEM reduced serum medium (51985034) and Cytiva HyClone™ Non-Essential Amino Acids 100× Solution (SH3023801) were purchased from Thermo Fisher Scientific. FBS (F0926, 500 mL), sodium bicarbonate (S6014, 500 g), DMSO (D8418-500ML), and Poly-L-lysine (PLL) (P4707-50mL) were purchased from MilliporeSigma. 8 well chambered cover glasses (Sterile, No. 1, C8-1-N and No. 1.5, C8-1.5-N) were ordered from Cellvis. Nucleofector 2b Kit V (VCA-1003) was purchased from LONZA. In Vivo mAb anti-human CD3 (OKT-3) (BE0001-2, 25 mg, Lot 809022M2) was purchased from BioXCell. Paraformaldehyde (15710) was purchased from Electron Microscopy Sciences. NHS-Biotin (2551), Sulfo-Cyanine3-NHS ester (11320) and Sulfo-Cyanine5-NHS ester (13320) were purchased from Lumiprobe. FITC anti-mouse CD8α Antibody (553030, Lot 2248217) was purchased from BD Biosciences. NEBuilder HiFi DNA Assembly (E2621G) was obtained from New England Biolabs. EasySep Mouse CD8+ T cell isolation kit (19853) and EasySep Mouse CD4+ T cell isolation kit (19852) were purchased from STEMCELL Technologies.

Cell culture
Jurkat E6.1 T cells (MilliporeSigma 88042803-1VL) were cultured in RPMI 1640 medium supplemented with 10% FBS and 100 units/mL penicillin-streptomycin. DC 2.4 cells (MilliporeSigma SCC142) were cultured in RPMI supplemented with 10% FBS, 100 units/mL penicillin-streptomycin, 1× HEPES, and 1× NEAA. HEK293T cells (ATCC, CRL-3216) were cultured in high-glucose DMEM supplemented with 10% FBS, 100 units/mL penicillin–streptomycin, 1 mM sodium pyruvate. U2OS cells (ATCC HTB-96) were cultured in DMEM supplemented with 10% FBS, 2 mM L-Glutamine, and 100 units/mL penicillin-streptomycin. All cell lines were maintained at 37 °C in a humidified atmosphere of 5% CO_2 and split at the confluence.

Preparation of coating surfaces for Jurkat T cells

Poly-L-lysine (PLL) surfaces were produced by adding 0.01% PLL. Stimulating surfaces were produced by adding an OKT-3 antibody at 1 μg/mL in DPBS *per* well. 8-well chambered cover glasses containing OKT-3 and PLL were incubated for 2 h at 37 °C in a humidified atmosphere of 5% CO_2.

NHS-ester labeling of cells in suspension

Cell suspensions were centrifuged in a benchtop centrifuge at 300 × g for 3 min at room temperature. Following centrifugation, the supernatant was carefully removed, leaving behind the cell pellets. These cell pellets were resuspended at a cell density of 2.0 × 10^5 cells/mL in 0.1 M $NaHCO_3$ (500 μL). Subsequently, the cell suspension was combined with a 0.5 μg/μL solution of NHS-ester dye (Alexa Fluor 647, Alexa Fluor 488, Sulfo-Cyanine3 or Sulfo-Cyanine5) in DMSO (50 μL). The reaction mixture was then gently rotated in darkness at room temperature for 3–5 min. To stop the reaction, 45 mg/mL of glycine in ultrapure water was added. To remove excess dye, the reaction mixture was centrifuged at 300 × g for 3 min at room temperature, after which the supernatant was discarded. The cells were then subjected to two wash cycles. Cells were resuspended in complete cell media (1 mL) and centrifuged at 300 × g for 3 min at room temperature. Following the washing steps, the labeled cells were resuspended in prewarmed complete cell media and appropriately diluted as required for subsequent cell seeding for experiments. Labeled cells were handled in a dark room under dim light.

DiO labeling

NHS-ester AF647 labeled cells (1.0 × 10^6 cells/mL, 1 mL) were incubated in 5 μM cell labeling solution in prewarmed serum-free cell media for 5 min at 37 °C in a humidified atmosphere of 5% CO_2. The cells were centrifuged and washed twice in prewarmed complete cell media.

Sample preparation for live-cell microscopy

DC2.4: Labeled cells were seeded at 5–10,000 cells per well and incubated for 1–2 h at 37 °C in a humidified atmosphere of 5% CO_2 before imaging. In dual-color experiments, cells were seeded at a 1:1 ratio. Jurkat T cells: Labeled Jurkat T cells were added onto PLL or OKT-3 coated glass slides at 80-100,000 cells per well on the microscope stage. Cell attachment was monitored with brightfield (~2 min) for live cell imaging, and the cell solution was aspirated and replaced with complete cell media. Time-lapse imaging was started immediately afterward.

DNA constructs

Plasmid constructs were obtained from Addgene. CAV1-mCherry was a gift from Ari Helenius (Addgene plasmid # 27705)[53]. mScarlet-Rab7 was a gift from Gia Voeltz (Addgene plasmid # 169068)[54]. mCherry-Lysosomes-20 (Addgene plasmid # 55073) and DsRed2-Mito-7 (Addgene plasmid # 55838) were gifts from Michael Davidson. InsR-EGFP was a gift from Joseph Bass, Northwestern University[55].

DC2.4 transfection

DC2.4 cells (1.0 × 10^6 cells) were electroporated with the plasmid (2 μg) using an Ingenio EZporator electroporation system. Cells were pulsed in 0.2 cm cuvettes at 150 V for 30 ms in the cell line nucleofector solution V (100 μL). Following 24 h after electroporation, cells were labeled in suspension, seeded onto 8-well chambered cover glass and imaged after 4 h of incubation at 37 °C in a humidified atmosphere of 5% CO_2.

Cloning of Cav1-mCherry constructs

To generate C-terminal-tagged mCherry Cav1-WT, and Cav1-Y14F constructs Cav1-WT, and Cav1-Y14F were amplified from the previously described Cav1-WT-CFP, Cav1-Y14F-YFP constructs[39]. The resulting PCR products were gel purified and assembled into the vector (Addgene plasmid # 27705)[53], previously digested with EcoRI and BamHI using NEBuilder HiFi DNA Assembly. All constructs were sequenced to confirm the presence of mutations. The following primer pair was used for PCR reactions.

Forward Primer:
5'-ACTCAGATCTCGAGCTCAAGCTTCGAATTCATGTCTGGGGGCAAATACGTAG-3'.

Reverse Primer:
5'-TTGCTCACCATGGTGGCGACCGTGGATCCTATTTCTTTCTGCAAGTTG ATGCGGATATT-3'.

Cav1 and InsR transfection and Insulin treatment of HEK293T cells

The insulin treatment procedure was adapted from Boothe et al.[37,38]. HEK293T cells were seeded at a density of 3 × 10^4 cells per well in low-glucose media (DMEM,1 g/L) supplemented with 10% FBS, and 100 units/mL of penicillin-streptomycin in a PLL-coated 8-well chambered cover glass 24 h before transfection. After reaching ~20–30% confluence, cells were transfected with plasmids InsR-EGFP (150 ng) and Cav1-mCherry (150 ng) pre-complexed with Lipofectamine 2000 at a ratio of 1:3 DNA:L2000 (w/v) in Opti-MEM reduced serum media for 15 min before adding dropwise to the cells. Transfection media was replaced with fresh low-glucose media after 4 h. After an additional 24–36 h, cells were starved in serum-free low-glucose DMEM for 2 h before labeling. sCy5-NHS-ester labeling was performed by replacing half of media with 40 μg/mL of sCy5-NHS-ester in 0.1 M $NaHCO_3$ (final concentration, 20 μg/mL) and incubating cells in dark for 3 min at room temperature. The reaction was quenched by adding glycine (4.5 mg/mL, 25 μL). The cells were washed two times with low glucose DMEM. Subsequently, media was replaced with low glucose DMEM containing 200 nM insulin and incubated for 1 h at 37 °C in a humidified atmosphere of 5% CO_2. Cells were fixed with 4% PFA in DPBS for 15 min and maintained in DPBS at 4 °C until imaging.

In vivo protein transfer

Splenocytes from a *SNF5*^{fl/fl} CD4-Cre^{+/-} mouse was harvested upon splenomegaly development. Single-cell suspension was generated for the adoptive transfer experiment. A total of 12.5 million bulk splenocytes were each labeled with sCy3 or sCy5 NHS-esters. The labeled cells were mixed, and 5 million cells were retro-orbitally injected into two 12 week-old male C57BL/6 mice. Splenocytes from the injected mice were harvested at 24 and 48 h post-injection. Single-cell suspensions were generated for further analysis. CD8+ and CD4+ Lymphoma T cells from mouse lymphoma splenocytes were isolated by immunomagnetic negative selection using EasySep Mouse CD8+ and EasySep Mouse CD4+ isolation kits according to manufacturer guidelines.

FITC-OVA treatment

DC2.4 cells labeled with sulfo-Cy5 and sulfo-Cy3 were incubated with 0.5 mg/mL FITC-OVA in complete growth media for 3 h at 37 °C in a humidified atmosphere of 5% CO_2.

Dynabead incubation

Labeled Jurkat T cells were added onto PLL-coated glass slides on the microscope stage. After monitoring cell attachment in brightfield (~2 min), the cell solution was replaced with complete cell media. The Dynabeads were used at a 1:1 ratio of Jurkat T cells to Dynabeads. The Dynabeads were washed with 1 mL of DBPS with 0.1% BSA (pH 7.4) supplemented with 2 mM EDTA. The Dynabeads were isolated from the washing solution by placing the Dynabead suspension in a 6-tube magnetic separation rack for 1 min. The supernatant was discarded, and the Dynabeads were resuspended in complete growth media

before addition to the sample well with Jurkat T cells immobilized onto PLL. Time-lapse imaging was started immediately afterward.

NHS-ester labeling of U2OS

U2OS cells were seeded at 10–20,000 cells per well and incubated for 36 h at 37 °C in a humidified atmosphere of 5% CO_2. The cells were washed twice with serum-free media. NHS-ester dye (sCy3, 0.5 µg/µL) in DMSO (50 µL) was combined with 0.1 M $NaHCO_3$ (500 µL). The dye mixture was added onto the coverglass with adherent cells and incubated in darkness at room temperature for 2 min. To stop the reaction, 45 mg/mL of glycine in ultrapure water was added. The solution was aspirated, and the cells were washed three times with complete growth media.

DiOC6(3) staining of DC2.4

DiOC6(3) solid was constituted in DMSO. Working aliquots of 1 µM DiOC6(3) were stored desiccated at -20 °C. DC2.4 cells were seeded at 5000 cells per well and cultured overnight at 37 °C and 5% CO_2. DiOC6(3) was added to the cell media to yield a final concentration of 5 nM. Time-lapse imaging was performed immediately afterward.

Cell surface labeling assessment with trypan blue

Trypan blue was added to the sample well to a final concentration of 1 mg/mL, incubated for 1 min at room temperature on stage, and was imaged immediately after.

Cell viability assessment

Labeled T cells and DC2.4 cells were grown overnight in corresponding complete cell media. The cell suspensions were diluted in trypan blue to a final concentration of 1 mg/mL and incubated for 1 min at room temperature. 10 µL of this solution was mounted on a glass slide and imaged immediately after.

Cell fixation for DeepSIM imaging

Labeled cells (DC2.4 ~5000 cells per well and Jurkat T cells ~60,000 cells per well) were seeded in chambered cover glasses. DC2.4 cells were incubated for 2–4 h at 37 °C in a humidified atmosphere of 5% CO_2. Jurkat T cells were incubated on corresponding coated surfaces for 30 min at 37 °C in a humidified atmosphere of 5% CO_2. Following incubation, cells were fixed with PFA (4%) in DPBS for 15 min at room temperature. Cells were maintained in DPBS at 4 °C until imaging.

Immunofluorescence staining

Splenocytes (100,000 cells per well) were landed on PLL-coated coverglass for 30 min. Cells were fixed with 4% PFA in DPBS for 15 min. Cells were immunostained overnight with FITC conjugated anti-CD8α antibody at 10 µg/mL. Cells were washed twice and imaged in DPBS.

Microscopy

Live cell imaging. TIRF microscopy was performed using ND acquisition in Nikon NIS-Elements Advanced Research software (Version: 5.42.06) on an inverted Nikon Ti2E microscope equipped with 100 × / 1.49 oil-immersion objective (CFI Apochromat TIRF 100XC), a quad-band TIRF set TRF89901-ET-405/488/561/640 nm (Chroma Technology) and emission filters ET450/50 m, ET525/50 m, ET600/50 m, ET700/75 m (Chroma Technology). Time-lapse movies with 10 s time intervals were recorded using a Prime 95B sCMOS camera (Serial Number: A21C203010) at 16-bit with 2 × 2-pixel binning (effective pixel size of 220 nm). An integration time of 50 ms was used with 640 nm, 561 nm, and 488 nm lasers at laser power densities 2, 1.5, and 10 W/cm^2, respectively. Movies were collected for 1–2 h as intended at room temperature.

Superresolution imaging. Superresolution imaging was performed using a DeepSIM (Crest Optics) system mounted on an inverted Nikon

Ti-2E microscope using a Kinetix sCMOS camera (Serial Number: A23H723002) and a Nikon 60 ×/1.42 (Plan Apochromat λD 60 × OIL OFN 25 DIC N2, 108 nm image pixel size) or 100 ×/1.49 oil immersion objective (CFI Apochromat TIRF 100XC, 65 nm image pixel size). Image acquisitions were performed using NIS-Elements Advanced Research software (Version: 5.42.06). Multiplex 2D-DeepSIM images were captured using the 'Deep Imaging' DeepSIM mode with 488, 561, and 640 nm laser illumination, using an integration time of 25-200 ms. Images captured with DeepSIM were reconstructed within NIS-Elements Software. Reconstructed image pixel sizes are 54 nm and 32 nm for images acquired with 60× and 100× objectives, respectively. 3D-DeepSIM images of fixed Jurkat T-cells were captured using the 'Standard' DeepSIM mode with 640 nm laser illumination, an integration time of 50 ms, and a step size of 0.5 µm. Live-cell volumetric movies of Jurkat T cells were captured using the 'High throughput' DeepSIM mode with 488 nm laser illumination, an integration time of 30 ms, a time-lapse of 30 s, and a step size of 0.5 µm. Image volumes were captured from bottom (coverglass surface, 0 µm) to top. Captured image volumes with DeepSIM were reconstructed within NIS-Elements Software, followed by blind 3D Deconvolution– blending: Depth-coded alpha (rainbow). The image contrasts of the 3D-rendered images were adjusted for each channel in the LUTs (Gamma value (G) = 1.00) followed by further adjustments over the z-depth in the 'Z-LUTs for Volume View' in NIS-Elements Advanced Research software (Version: 5.42.06).

Brightfield imaging of trypan blue-stained cells. Images were taken using a TS-2R microscope with a 10x/0.25 objective (Plan 10 × Ph1 DL).

Data processing

TIRF microscopy images and 2D DeepSIM images were visualized and analyzed using ImageJ (Fiji) 1.54 f. Volumetric DeepSIM movies (Supplementary Movies 10–13, and 15) created within NIS-Elements Advanced Research software (Version: 5.42.06) were exported and mp4 files were generated in iMovie (v10.4.3) with normal playback speed.

Single particle tracking was performed using the 'Track Binaries' analysis option in the 2D tracking module of NIS-Elements Advanced Research software (Version 5.21.03). Membrane-derived particles were selected based on the intensity, and binary masks were created. Objects were tracked using the 'Random Motion' model, at maximum speed, with intensity (bright)-based centroid calculation. A standard deviation multiplication factor of 3.5 was used to track individual objects. Tracks were linked with 5 maximum gaps allowed. Tracks with three or fewer frames were removed.

Colocalization analysis was done using the 'colocalization' tool in NIS-Elements Advanced Research software (Version 5.21.03). A region of interest was chosen per cell to best capture the intracellular membrane labeling signal (green) with the transfections (magenta). All ROIs used in this analysis are shown in Supplementary Figs. 5–8. Background subtraction was performed on each frame before the analysis.

Diameters of EVs were measured at the maximum width in ImageJ (Fiji) 1.54 f. For EVs <300 nm, the full width at half maximum (FWHM) was calculated following a Gaussian fitting to the intensity line profile in OriginPro 2022 (9.9.0.225, Academic).

Protein enrichment and LC-MS/MS analysis

DC 2.4 cells were seeded in 10-cm Petri dishes and left to attach and grow. Cells were washed twice with cold PBS and incubated with cold PBS containing either DMSO or NHS-Biotin (100 µM) for 1 h at 4 °C. Cells were washed once with cold PBS, scrapped, and centrifuged at 1500 × g for 5 min at 4 °C. Cell pellets were resuspended in 500 µL PBS and cells were broken using a 28 G needle (10 strokes). Samples were centrifuged at 700 × g for 5 min at 4 °C and supernatants were transferred to a new microtube. Supernatants were then centrifuged at

17,000 × g for 15 min at 4 °C and new supernatants were transferred to a new microtube. Finally, supernatants were centrifuged at 100,000 × g for 60 min at 4 °C. Pellets were washed once with PBS and resuspended in PBS via sonication. Protein concentration was determined using the Bradford assay. For the identification of NHS-biotin-bound proteins, lysates (1 mg, 5 mL) in 0.2% SDS in PBS were incubated with 100 μL magnetic streptavidin beads (Promega) for 4 h at room temperature with rotation. Beads were washed with 1% SDS in PBS (1 time in 10 mL), transferred to microtubes, and washed with PBS (3 times in 1 mL), and water (3 times in 1 mL). Beads were resuspended in 6 M urea in PBS (500 μL), reduced with 10 mM neutralized TCEP (20× fresh stock in water) for 30 min at room temperature, and alkylated with 25 mM iodoacetamide (400 mM fresh stock in water) for 30 min at room temperature in the dark. Beads were resuspended in 150 μL of 2 M Urea, 1 mM $CaCl_2$ (100× stock in water), and trypsin (Thermo Scientific, 1 μL of 0.5 μg/μL) in 50 mM NH_4HCO_3. The digestion was performed overnight at 37 °C with shaking at 1500 rpm. For the identification of total proteins, lysate (20 μg) in PBS was denatured with 6 M urea in 50 mM NH_4HCO_3, reduced with 10 mM neutralized TCEP (20 × fresh stock in water) for 30 min at room temperature, and alkylated with 25 mM iodoacetamide (400 mM fresh stock in water) for 30 min at room temperature in the dark. Urea was diluted to 2 M with 50 mM NH_4HCO_3 and proteins were digested with trypsin (1 μL of 0.5 μg/μL) in the presence of 1 mM $CaCl_2$ (100 × stock in water) overnight at 37 °C with shaking at 1500 rpm. Samples were acidified with 1 vol. of isopropanol 1% TFA and desalted using styrene divinylbenzene reverse-phase sulfonate (SDB-RPS) StageTips[56]. Samples were loaded on a 200 μL StageTip containing two SDB-RPS disks and centrifuged at 1500 × g for 12 min. StageTips were washed three times with 200 μL of isopropanol 1% TFA at 1500 × g for 7 min, then eluted with 100 μL of 80% MeCN, 19% water, and 1% ammonia and dried. Peptides were resuspended in water with 0.1 % formic acid (FA) and analyzed using nanoElute 2 coupled to a TimsTOF HT mass spectrometer (Bruker Daltonics). The chromatography column consisted of a 25 cm long, 150 μm i.d. microcapillary packed with 1.5 μm C18 particles (Bruker Daltonics/Pepsep) and was capped by a 20 μm emitter (Bruker Daltonics). LC solvents were 0.1 % FA in H_2O (Buffer A) and 0.1 % FA in MeCN (Buffer B). Peptides were eluted into the MS at a flow rate of 500 nL/min. over a 60 min. linear-gradient (5-35 % Buffer B) at 50 °C. Data was acquired via dda-PASEF using 10 PASEF ramps per one MS1 scan and fragmented ions with charges 0–5. The method covered m/z 100-1700 and scan range between 0.6–1.6 1/K0. Ramp time was set to 100 ms and the total cycle lasted 1.17 s. Collision energy was set as a linear increase from 20 eV at 1/K0 = 0.6 to 59 eV at 1/K0 = 1.6. Data was acquired as n = 3 technical replicates for each condition.

Fragpipe analysis
The MS data was analyzed with Fragpipe (V22)[57,58] and searched against the *Mus musculus* proteome (Uniprot UP000000589) and a common list of contaminants (included in Fragpipe). Peptide and fragment mass tolerance was set to 20 ppm. The minimum peptide length was set to 6 amino acids with a mass range of 500 to 5000 Da. Trypsin was used as protease with up to 2 missed cleavages. Carbamidomethylation of cysteine was set as a fixed modification and oxidation of methionine and N-terminal acetylation as variable modifications. PSM validation was performed with Percolator. Quantification was performed using IonQuant with MBR and MaxLFQ enabled and without normalization. Mouse plasma membrane proteins were extracted using the GO term 0005886. A 4-fold threshold of NHS-Biotin over DMSO was applied for proteins to be considered as enriched.

Statistics and reproducibility
No statistical method was used to predetermine sample size. No data were excluded from the analyses. The experiments were not randomized. The investigators were not blinded to allocation during experiments and outcome assessment. For reproducibility, all experiments were repeated independently at least three times, unless otherwise noted.

Reporting summary
Further information on research design is available in the Nature Portfolio Reporting Summary linked to this article.

Data availability
The mass spectrometry data generated in this study have been deposited to the ProteomeXchange Consortium via the PRIDE partner repository with the dataset identifier PXD061317. The MS data was analyzed with Fragpipe (V22)(Yu et al[57].; Yu et al[58].) and searched against the *Mus musculus* proteome in Uniprot (UP000000589, https://www.uniprot.org/proteomes/UP000000589, downloaded December 2024) and a common list of contaminants (included in Fragpipe). Imaging datasets generated and used in this study are available from the corresponding author upon request. Source data are provided with this paper.

References
1. Armingol, E., Officer, A., Harismendy, O. & Lewis, N. E. Deciphering cell–cell interactions and communication from gene expression. *Nat. Rev. Genet.* **22**, 71–88 (2020).
2. Cordero Cervantes, D. & Zurzolo, C. Peering into tunneling nanotubes—the path forward. *EMBO J.* **40**, e105789 (2021).
3. Rustom, A., Saffrich, R., Markovic, I., Walther, P. & Gerdes, H.-H. Nanotubular highways for intercellular organelle transport. *Science* **303**, 1007–1010 (2004).
4. Buzas, E. I. The roles of extracellular vesicles in the immune system. *Nat. Rev. Immunol.* **23**, 236–250 (2022).
5. Kolba, M. D. et al. Tunneling nanotube-mediated intercellular vesicle and protein transfer in the stroma-provided imatinib resistance in chronic myeloid leukemia cells. *Cell Death Dis.* **10**, 817 (2019).
6. Rother, N., Yanginlar, C., Pieterse, E., Hilbrands, L. & van der Vlag, J. Microparticles in autoimmunity: cause or consequence of disease? *Front. Immunol.* **13**, 822995 (2022).
7. Panda, B., Sharma, Y., Gupta, S. & Mohanty, S. Mesenchymal stem cell-derived exosomes as an emerging paradigm for regenerative therapy and nano-medicine: a comprehensive review. *Life (Basel, Switz.).* **11**, 784 (2021).
8. Lotze, J., Reinhardt, U., Seitz, O. & Beck-Sickinger, A. G. Peptide-tags for site-specific protein labelling in vitro and in vivo. *Mol. Biosyst.* **12**, 1731–1745 (2016).
9. Erdmann, R. S. et al. Labeling strategies matter for super-resolution microscopy: a comparison between HaloTags and SNAP-tags. *Cell Chem. Biol.* **26**, 584–592.e6 (2019).
10. Chamma, I. et al. Mapping the dynamics and nanoscale organization of synaptic adhesion proteins using monomeric streptavidin. *Nat. Commun.* **7**, 10773 (2016).
11. Saka, S. K. et al. Multi-protein assemblies underlie the mesoscale organization of the plasma membrane. *Nat. Commun.* **5**, 4509 (2014).
12. Mateos-Gil, P., Letschert, S., Doose, S. & Sauer, M. Super-resolution imaging of plasma membrane proteins with click chemistry. *Front. Cell Dev. Biol.* **4**, 98 (2016).
13. Hassdenteufel, S. & Schuldiner, M. Show your true color: mammalian cell surface staining for tracking cellular identity in multiplexing and beyond. *Curr. Opin. Chem. Biol.* **66**, 102102 (2022).
14. Anderson, G. W., Zimmerman, J. E. & Callahan, F. M. The use of esters of N-hydroxysuccinimide in peptide synthesis. *J. Am. Chem. Soc.* **86**, 1839–1842 (2002).
15. M'Saad, O. & Bewersdorf, J. Light microscopy of proteins in their ultrastructural context. *Nat. Commun.* **11**, 1–15 (2020).
16. Han, Y. et al. A labeling strategy for living specimens in long-term/super-resolution fluorescence imaging. *Front. Chem.* **8**, 601436 (2020).

17. de Pedro, M. A., Young, K. D., Höltje, J.-V. & Schwarz, H. Branching of Escherichia coli cells arises from multiple sites of inert peptidoglycan. *J. Bacteriol.* **185**, 1147–1152 (2003).

18. Ge, X. et al. Live mapping of the brain extracellular matrix and remodeling in neurological disorders. *Small Methods* **8**, e2301117 (2024).

19. Fischer, A. et al. In vivo fluorescent labeling and tracking of extracellular matrix. *Nat. Protoc.* **18**, 2876–2890 (2023).

20. Lehmann, T. P. et al. Quantification of the asymmetric migration of the lipophilic dyes, DiO and DiD, in homotypic co-cultures of chondrosarcoma SW-1353 cells. *Mol. Med. Rep.* **14**, 4529 (2016).

21. Han, Y., Li, M., Qiu, F., Zhang, M. & Zhang, Y.-H. Cell-permeable organic fluorescent probes for live-cell long-term super-resolution imaging reveal lysosome-mitochondrion interactions. *Nat. Commun.* **8**, 1307 (2017).

22. Altuzar, J. et al. Lysosome-targeted multifunctional lipid probes reveal the sterol transporter NPC1 as a sphingosine interactor. *Proc. Natl Acad. Sci. Usa.* **120**, e2213886120 (2023).

23. Ren, X. et al. Current lipid extraction methods are significantly enhanced adding a water treatment step in chlorella protothecoides. *Microb. Cell Fact.* **16**, 1–13 (2017).

24. Zaccard, C. R. et al. CD40L induces functional tunneling nanotube networks exclusively in dendritic cells programmed by mediators of type-1 immunity. *J. Immunol.* **194**, 1047 (2014).

25. Gerdes, H.-H., Bukoreshtliev, N. V. & Barroso, J. F. V. Tunneling nanotubes: a new route for the exchange of components between animal cells. *FEBS Lett.* **581**, 2194–2201 (2007).

26. Onfelt, B. et al. Structurally distinct membrane nanotubes between human macrophages support long-distance vesicular traffic or surfing of bacteria. *J. Immunol.* **177**, 8476–8483 (2006).

27. Jing, H. et al. Fluorescent artificial antigens revealed extended membrane networks utilized by live dendritic cells for antigen uptake. *Nano Lett.* **22**, 4020–4027 (2022).

28. Stewart, D. et al. Stable and ordered amide frameworks synthesised under reversible conditions which facilitate error checking. *Nat. Commun.* **8**, 1102 (2017).

29. Garrett, W. S. et al. Developmental control of endocytosis in dendritic cells by Cdc42. *Cell* **102**, 325–334 (2000).

30. Shakushiro, K., Yamasaki, Y., Nishikawa, M. & Takakura, Y. Efficient scavenger receptor-mediated uptake and cross-presentation of negatively charged soluble antigens by dendritic cells. *Immunology* **112**, 211–218 (2004).

31. Dubois, F. et al. Investigating tunneling nanotubes in cancer cells: guidelines for structural and functional studies through cell imaging. *BioMed. Res. Int.* **2020**, 2701345 (2020).

32. Abounit, S., Delage, E. & Zurzolo, C. Identification and characterization of tunneling nanotubes for intercellular trafficking. *Curr. Protoc. Cell Biol.* **67**, 12.10.1–12.10.21 (2015).

33. Galbiati, F., Razani, B. & Lisanti, M. P. Emerging themes in lipid rafts and caveolae. *Cell* **106**, 403–411 (2001).

34. Yang, Y., Xin, Z., Chu, J., Li, N. & Sun, T. Involvement of Caveolin-1 in CD83 internalization in mouse dendritic cells. *Cell Transplant.* **24**, 1395–1404 (2015).

35. Werling, D. et al. Involvement of caveolae in the uptake of respiratory syncytial virus antigen by dendritic cells. *J. Leukoc. Biol.* **66**, 50–58 (1999).

36. Harris, J. et al. Expression of caveolin by bovine lymphocytes and antigen-presenting cells. *Immunology* **105**, 190–195 (2002).

37. Boothe, T. et al. Inter-domain tagging implicates caveolin-1 in insulin receptor trafficking and Erk signaling bias in pancreatic beta-cells. *Mol. Metab.* **5**, 366–378 (2016).

38. Boothe, T. et al. Corrigendum to 'Inter-domain tagging implicates caveolin-1 in insulin receptor trafficking and Erk signaling bias in pancreatic beta-cells' [Mol Metab 2016 May; 5 (5): 366-378]. *Mol. Metab.* **83**, 101935 (2024).

39. Zimnicka, A. M. et al. Src-dependent phosphorylation of caveolin-1 Tyr-14 promotes swelling and release of caveolae. *Mol. Biol. Cell* **27**, 2090–2106 (2016).

40. Goetz, J. G., Lajoie, P., Wiseman, S. M. & Nabi, I. R. Caveolin-1 in tumor progression: the good, the bad and the ugly. *Cancer Metastasis Rev.* **27**, 715–735 (2008).

41. Kim, H.-R. et al. T cell microvilli constitute immunological synaptosomes that carry messages to antigen-presenting cells. *Nat. Commun.* **9**, 3630 (2018).

42. Blanchard, N. et al. TCR activation of human T cells induces the production of exosomes bearing the TCR/CD3/zeta complex. *J. Immunol.* **168**, 3235–3241 (2002).

43. Wang, X. et al. TCR-dependent transformation of mature memory phenotype T cells in mice. *J. Clin. Invest.* **121**, 3834–3845 (2011).

44. Geng, X. et al. GATA-3 is a proto-oncogene in T-cell lymphoproliferative neoplasms. *Blood Cancer J.* **12**, 149 (2022).

45. Harshyne, L. A., Watkins, S. C., Gambotto, A. & Barratt-Boyes, S. M. Dendritic cells acquire antigens from live cells for cross-presentation to CTL. *J. Immunol.* **166**, 3717–3723 (2001).

46. Saha, T. et al. Intercellular nanotubes mediate mitochondrial trafficking between cancer and immune cells. *Nat. Nanotechnol.* **17**, 98–106 (2022).

47. Baldwin, J. G. et al. Intercellular nanotube-mediated mitochondrial transfer enhances T cell metabolic fitness and antitumor efficacy. *Cell* **187**, 6614–6630.e21 (2024).

48. Wang, X. & Gerdes, H.-H. Transfer of mitochondria via tunneling nanotubes rescues apoptotic PC12 cells. *Cell Death Differ.* **22**, 1181–1191 (2015).

49. Notario Manzano, R. et al. Proteomic landscape of tunneling nanotubes reveals CD9 and CD81 tetraspanins as key regulators. *eLife* **13**, RP99172 (2024).

50. Zhang, L. et al. Wheat germ agglutinin-conjugated fluorescent pH sensors for visualizing proton fluxes. *J. Gen. Physiol.* **152**, e201912498 (2020).

51. Chen, L., Ma, L. & Yu, L. WGA is a probe for migrasomes. *Cell Discov.* **5**, 13 (2019).

52. Lassailly, F., Griessinger, E. & Bonnet, D. Microenvironmental contaminations' induced by fluorescent lipophilic dyes used for noninvasive in vitro and in vivo cell tracking. *Blood* **115**, 5347–5354 (2010).

53. Hayer, A., Stoeber, M., Bissig, C. & Helenius, A. Biogenesis of caveolae: stepwise assembly of large caveolin and cavin complexes. *Traffic* **11**, 361–382 (2010).

54. Wu, H. & Voeltz, G. K. Reticulon-3 promotes endosome maturation at ER membrane contact sites. *Dev. Cell* **56**, 52–66.e7 (2021).

55. Ramos, R. R., Swanson, A. J. & Bass, J. Calreticulin and Hsp90 stabilize the human insulin receptor and promote its mobility in the endoplasmic reticulum. *Proc. Natl Acad. Sci. USA* **104**, 10470–10475 (2007).

56. Brunner, A.-D. et al. Ultra-high sensitivity mass spectrometry quantifies single-cell proteome changes upon perturbation. *Mol. Syst. Biol.* **18**, e10798 (2022).

57. Yu, F. et al. Fast quantitative analysis of timsTOF PASEF data with MSFragger and IonQuant. *Mol. Cell. Proteom.* **19**, 1575–1585 (2020).

58. Yu, F., Haynes, S. E. & Nesvizhskii, A. I. IonQuant enables accurate and sensitive label-free quantification with FDR-controlled match-between-runs. *Mol. Cell. Proteom.* **20**, 100077 (2021).

Acknowledgements

Author contributions

H.G. and Y.S.H. conceived the work. H.G. designed and planned the experiments, performed cell culture, labeling, microscopy, and data analysis. Y.-S.C. assisted in experimental design, NHS-ester vacuum drying, performed cell culture, transfections, insulin treatment, cell labeling, and fixation. V.P.-S. and A.Z.-M. performed mouse dissection, cell transfer, and splenocyte single-cell suspension preparations. D.A. performed MS data analysis and visualization. A.B. performed mycoplasma testing. L.-W.G., A.A., C.M.-Z. and A.E.O. provided guidance on experimental designs. Y.S.H. acquired funding and provided supervision on experimental design and data analysis. H.G. and Y.S.H. drafted the manuscript, and all reviewed and edited the manuscript.

Competing interests

The authors declare no competing interests.

Additional information

Supplementary information The online version contains supplementary material available at
https://doi.org/10.1038/s41467-025-58779-2.

Correspondence and requests for materials should be addressed to Ying S. Hu.

Peer review information *Nature Communications* thanks Yuval Rinkevich and the other, anonymous, reviewer(s) for their contribution to the peer review of this work. A peer review file is available.

Reprints and permissions information is available at
http://www.nature.com/reprints

Publisher's note Springer Nature remains neutral with regard to jurisdictional claims in published maps and institutional affiliations.